NJC

ROYAL SOCIETY OF CHEMISTRY

PAPER

Cite this: *New J. Chem.*, 2021, **45**, 17266

A renewable photocatalytic system with dramatic photocatalytic activity for H_2 evolution and constant light energy utilization: eosin Y sensitized $ZnWO_4$ nanoplates loaded with CuO nanoparticles†

Xiaoluo Bao,[a] Xiaokun Wang,[a] Xiangqing Li,[a] Lixia Qin,[a] Taiyang Zhang,[a] Dewen Zheng,[b] Xi Zhang,[b] Jianming Li,[b] Shanyu Wang[b] and Shi-Zhao Kang*[a]

Received 23rd June 2021,
Accepted 16th August 2021

DOI: 10.1039/d1nj03070a

rsc.li/njc

It is necessary for the commercialization of sunlight-driven H_2 evolution to develop an efficient photocatalytic system whose energy utilization is independent of incident light intensity. Unfortunately, limited attention has been paid to the effect of light intensity on energy utilization. For all the above reasons, a photocatalytic system made up of eosin Y, $ZnWO_4$ nanoplates and CuO nanoparticles was fabricated. Meanwhile, its photocatalytic activity for H_2 evolution was evaluated under illumination with various light intensities. In light of the experimental results, we can conclude that the aforementioned system possesses dramatic photocatalytic performance for H_2 evolution. Under strong illumination (100 mW cm^{-2}), the highest H_2 evolution rate is as high as 4.9 mmol g^{-1} h^{-1}. Even if under weak illumination (10 mW cm^{-2}), the H_2 evolution rate is still 0.53 mmol g^{-1} h^{-1}. More interesting, the energy utilization of this system is independent of light intensity. These results might provide some new ideas for the design and preparation of high-efficiency photocatalysts with light intensity-independent energy utilization.

Introduction

During recent decades, photocatalytic water-splitting has been a research hotspot as a promising technique to convert solar energy into environmentally friendly and storable chemical energy, *i.e.*, hydrogen fuels. Numerous efficient and economical photocatalysts have been developed, such as CdS nanosheets,[1] $ZnIn_2S_4$/Co-doped NH_2-MIL-53(Fe) nanocomposites,[2] a Ni_2P modified two-dimensional $SnNb_2O_6$/CdS–diethylenetriamine system,[3] Erythrosin B sensitized VB_2,[4] metal–organic framework-derived heterojunctions,[5] nanolayered heterostructures of N-doped TiO_2 and N-doped carbon,[6] Ag-decorated TiO_2 inverse opal structures,[7] Ba–P co-doped g-C_3N_4 microtubes,[8] Zn–$AgIn_5S_8$ quantum dot/NiS nanosheet nanocomposites,[9] g-C_3N_4 co-modified with graphene and NiS,[10] and so on. However, the effect of light intensity on the energy utilization of the photocatalysts was neglected in the previous studies. There are limited papers on photocatalysts whose energy utilization is independent of incident light intensity. It is well known that sunlight intensity is unstable. From the viewpoint of application, an efficient photocatalytic system with light intensity-independent energy utilization is very desirable. Therefore, it is meaningful to prepare an efficient photocatalyst and evaluate its photocatalytic performance for H_2 generation under illumination with various light intensities.

Recently, some scientists found that, generally, the photocatalytic reaction has combined orders of 0.5 and 2 for incident photons.[11,12]

$$r \approx k_{cr}{\cdot}P^{0.5} + k_{te}{\cdot}P^2 \qquad (1)$$

where r is the rate of the photocatalytic reaction, k_{cr} is the constant for trap-states-intermediated charge recombination, k_{te} is the constant for thermionic emission, and P is the incident photons. Under weak irradiation, r is approximately proportional to the square root of P. In contrast, r is approximately proportional to the square of P under strong irradiation.[11,12] Thus, the light energy utilization of photocatalysts would reach a minimum when the light intensity changes. To avoid this problem, the activation energy of interfacial electron transfer

---

[a] School of Chemical and Environmental Engineering, Shanghai Institute of Technology, 100 Haiquan Road, Shanghai 201418, China. E-mail: kangsz@sit.edu.cn; Fax: +86 21 60873061; Tel: +86 21 60873061

[b] New Energy Research Center, Research Institute of Petroleum Exploration & Development (RIPED), PetroChina, 20 XueYuan Road, Beijing 100083, China

† Electronic supplementary information (ESI) available. See DOI: 10.1039/d1nj03070a

ought to be reduced. If the energy barriers are narrowed, the photocatalytic reaction would be quasi-first-order towards P.

$$r \approx k \cdot P \tag{2}$$

where k is the constant for interfacial electron transfer. The light energy utilization of a photocatalyst would remain constant even if the light intensity changes. The theoretical prediction[12] indicates that it is possible to fabricate a photocatalytic system whose energy utilization is independent of incident light intensity if we can introduce efficient tunneling in the photocatalytic system. However, it is a challenge because a high concentration of electronic doping is needed to achieve efficient tunneling in photocatalytic systems.

Dye sensitization has been regarded as an efficient method to broaden the light absorption of photocatalysts.[13–17] The results reported preciously indicate that in a dye sensitized photocatalytic system, the sensitizer efficiently absorbs light and its electrons are excited under irradiation. Afterwards, these excited electrons can migrate to the conduction band of a semiconductor. Thus, the concentration of electron on the surface of the semiconductor will increase. Simultaneously, the Fermi energy level of the semiconductor would rise, which would lead to reduction of the potential barrier of interfacial electron transfer.[18,19] Therefore, it can be speculated that efficient tunneling could be achieved in a dye sensitized photocatalytic system. On the other hand, dyes usually possess very high molar absorption coefficients. This will guarantee that the photocatalytic system can absorb enough light to bring forth photo-induced electrons even if under weak illumination. So, we can deduce that it is feasible to prepare a high-efficiency photocatalyst with light intensity-independent energy utilization *via* dye sensitization.

Due to excellent thermal/chemical stability, non-toxicity, high refractive index, high quantum yield and relatively low cost, $ZnWO_4$ has been accepted as a candidate with great promise in the field of photocatalysis. $ZnWO_4$-based photocatalysts were extensively explored for photocatalytic hydrogen production and removal of inorganic/organic contaminants.[20–27] The experimental results confirm that the photocatalytic performance of $ZnWO_4$ can be strikingly boosted through dye sensitization. On the other hand, Eosin Y (EY) has been widely used to broaden the light absorption range of photocatalytic systems as a sensitizer with all-round excellent properties. A lot of efficient photocatalysts have been developed utilizing the sensitization of EY, such as the photocatalytic system containing a g-C_3N_4/GO hybrid, EY and Pt–Ni cocatalyst,[28] manganese incorporated EY/graphene nanocomposites,[29] EY-sensitized Ni(II) complexes of pyridylbenzimidazole,[30] EY-sensitized Co@boron nitride core–shell composites,[31] carbon nitride/cobalt ion/eosin Y nanohybrids,[32] EY-sensitized MoS_2 nanomesh,[33] EY-sensitized Ag@Ag–Pd alloy catalysts,[34] a photocatalytic system containing EY, Ni_2P/Ni nanoparticles and C/g-C_3N_4 hybrids,[35] and EY-sensitized UiO-66-NH_2.[36] According to the above results, it is rational to speculate that the EY sensitized $ZnWO_4$-based photocatalytic system might exhibit not only high photocatalytic activity but also light intensity-independent energy utilization. However, it is still unclear whether the EY sensitized $ZnWO_4$-based photocatalyst is an efficient photocatalytic system whose energy utilization is independent on incident light intensity for H_2 evolution or not. So, it is essential to prepare a photocatalytic system made up of EY and $ZnWO_4$, and investigate the effect of light intensity on its photocatalytic performance for H_2 generation.

Moreover, in order to restrain recombination of the electron–hole pair efficiently, a co-catalyst is often introduced into the photocatalytic system. Recent studies show that CuO is an efficient co-catalyst for various semiconductors, including TiO_2,[37] Bi_2MoO_6,[38] ZnO,[39] $CuWO_4$,[40] $BiVO_4$,[41] g-C_3N_4,[42] *etc.* Therefore, we can speculate that the photocatalytic performance of the EY sensitized $ZnWO_4$-based photocatalyst should be distinctly boosted due to introduction of CuO. Based on the above considerations, we prepared a photocatalytic system made up of Eosin Y, $ZnWO_4$ nanoplates and CuO nanoparticles (EY–$ZnWO_4$/CuO). Then, its photocatalytic activity was evaluated for H_2 generation under illumination with various light intensities. Finally, the photocatalytic mechanism was probed roughly.

Experimental

Preparation of $ZnWO_4$ nanoplates

$ZnWO_4$ nanoplates were prepared in a hydrothermal process (Scheme 1). Typically, $Zn(NO_3)_2 \cdot 6H_2O$ (10 mmol) was dissolved in redistilled water (15 mL). Next, 1 mmol of cetyltrimethyl ammonium bromide (CTAB) was introduced into the aforementioned solution. Subsequently, the blend was stirred for 60 min to obtain solution A. Similarly, 10 mmol of $NaWO_4$ was dissolved in deionized water (15 mL) under stirring to obtain solution B. After solution B was slowly mixed with solution A under stirring, the blend was transferred into a Teflon container (60 mL). Next, the container was enclosed with an autoclave and heated at 180 °C for 20 h. After the temperature of the autoclave dropped to room temperature, the precipitate was taken out with a centrifuge and then washed thoroughly with water. At last, the solid obtained was desiccated at 80 °C for 24 h.

Preparation of $ZnWO_4$ nanoplates loaded with CuO nanoparticles ($ZnWO_4$/CuO)

Firstly, the as-prepared $ZnWO_4$ nanoplates (500 mg) were dispersed in deionized water (30 mL). Secondly, $Cu(NO_3)_2 \cdot 3H_2O$ (95 mg) was mixed with the aforementioned suspension. Then, the temperature of the blend rose to 75 °C. Thirdly, the pH value was adjusted to 10 using ammonium hydroxide at 75 °C. Afterwards, the temperature of the suspension was kept at 75 °C for 2 h under stirring. After the temperature of the suspension dropped to room temperature, the precipitate was taken out by centrifugation, washed thoroughly with water and isopropyl alcohol, and desiccated at 80 °C for 6 h. Finally, the solid was calcined at 200 °C for 1 h in an air atmosphere. In the present work, the products are denoted as $ZnWO_4$/CuO (x%). Therein, x% is the content of CuO.

Photocatalytic activity test

The photocatalytic activity tests were carried out in a top-irradiation quartz reactor with a circulating water jacket at

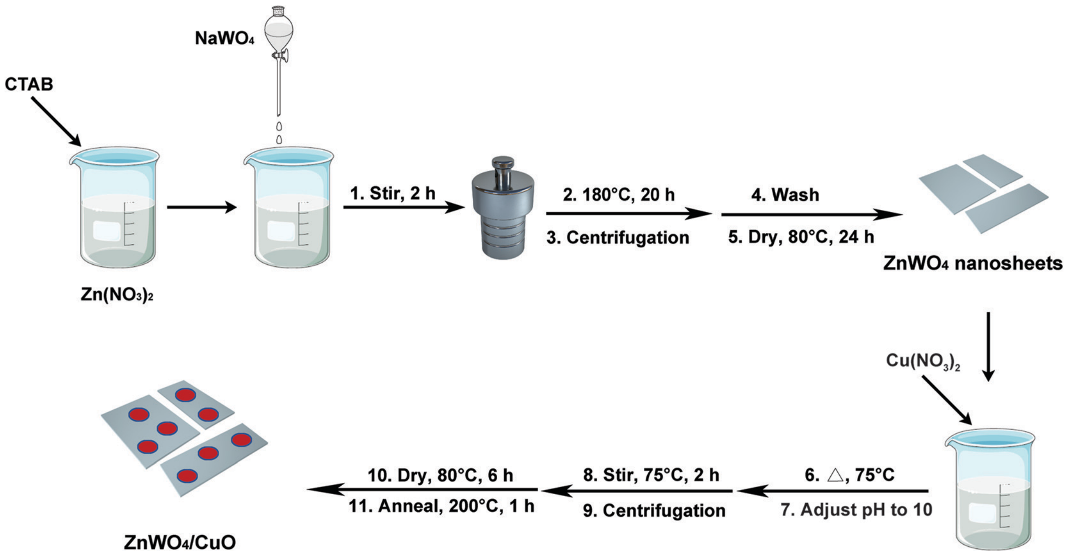

Scheme 1 Schematic diagram of the synthetic process of $ZnWO_4$/CuO.

10 °C. A 500 W Hg lamp served as the light source and was placed 1 cm away from the reactor. A certain light density of incident light was set and calibrated with a Ceaulight CEL-NP2000 light intensity meter (China). In a typical experiment, $ZnWO_4$/CuO (6%) (5 mg) was put in a reactor containing water (55 mL) under stirring. Then, EY (40 mg) was introduced into the reactor. After the blend was stirred for 1 h in the dark, triethanolamine (TEOA, 5 mL) was added into the above suspension. Before irradiation, N_2 was injected into the reactor for 5 min. At last, the Hg lamp was turned on. The light density of incident light was adjusted and measured. After irradiating for some time, the hydrogen production was detected with gas chromatography (molecular sieve 5A, TCD, carrier gas N_2). The H_2 evolution rate (V) and the energy utilization factor (EUF) were calculated according to the following equations:

$$V = \text{the amount of hydrogen produced}/(m \times t) \quad (3)$$

$$\text{EUF} = \text{the amount of hydrogen produced}/(m \times t \times I \times S) \quad (4)$$

where m is the mass of $ZnWO_4$/CuO, t is the irradiation time, I is the light density of incident light and S is the irradiated area.

Using monochromatic light (450 nm, 57.1 mW cm^{-2}) as a light source, the average hydrogen evolution rate was measured after irradiating for 4 h. Then, the quantum yield (QE) of EY–$ZnWO_4$/CuO was calculated according to the equation below:

$$\begin{aligned}\text{QE} &= \text{number of reacted electrons/number of incident photons} \times 100\% \\ &= 2 \times \text{number of evolved } H_2 \text{ molecules/number of incident photons} \times 100\% \\ &= 2vtN_A/(IStl\lambda(1/hc)) \times 100\%\end{aligned} \quad (5)$$

where ν is the average hydrogen evolution rate (mol s^{-1}), t is the irradiation time (s), N_A is Avogadro's constant 6.022×10^{23} (mol^{-1}), I is the light density of incident light (W cm^{-2}), S is the irradiation area (cm^2), λ is the wavelength of incident light (m), h is Planck's constant 6.626×10^{-34} (J s) and c is the speed of light 3×10^8 m s^{-1}.

The solar-to-hydrogen (STH) conversion efficiency of EY–$ZnWO_4$/CuO was calculated according to the equation below.

$$\text{STH} = \nu\Delta Gr/(IS) \times 100\% \quad (6)$$

where ν is the average hydrogen evolution rate (mol s^{-1}), ΔGr is the Gibbs energy for $H_2O(l) \rightarrow H_2(g) + 1/2O_2(g)$ (286 kJ mol^{-1}), I is the light density of incident light (W cm^{-2}) and S is the irradiated sample area (cm^2).

Photoelectrochemical measurements

The photoelectrochemical measurements were carried out in a three-electrode cell with a CHI660E electrochemical workstation. A piece of fluorine-doped tin oxide (FTO) glass coated with $ZnWO_4$/CuO, Ag/AgCl electrode and platinum wire electrode acted as the working electrode, the reference electrode, and the counter electrode, respectively. A 300 W Xe lamp served as the light source and was placed 7 cm away from the cell. The supporting electrolyte used was Na_2SO_4 aqueous solution (0.2 mol L^{-1}).

Results and discussion

Characterization of $ZnWO_4$/CuO

The X-ray diffraction (XRD) patterns of the $ZnWO_4$ nanoplates, the CuO nanoparticles and $ZnWO_4$/CuO (6%) are shown in Fig. 1. From the XRD pattern of the $ZnWO_4$ nanoplates, we can clearly observe several sharp XRD diffraction peaks, suggesting that the sample possesses high crystallization. These diffraction peaks are well indexed to monoclinic $ZnWO_4$ with the standard

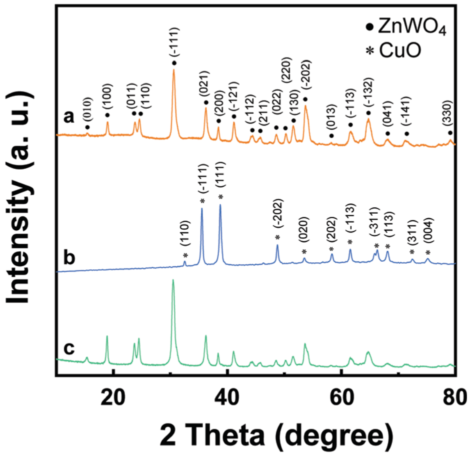

Fig. 1 XRD patterns of (a) the $ZnWO_4$ nanoplates, (b) the CuO nanoparticles and (c) $ZnWO_4$/CuO (6%).

card (JCPDS No. 89-0447).[43] Three of the strongest peaks can be assigned to the (−111), (−202) and (021) planes of monoclinic $ZnWO_4$, respectively. Moreover, no diffraction peaks ascribed to other impurities can be found. This result indicates that the as-prepared product is monoclinic $ZnWO_4$. Similarly, the diffraction peaks of $ZnWO_4$/CuO (6%) also match well with the standard pattern of monoclinic $ZnWO_4$ (JCPDS No. 89-0447), and we can observe that the diffraction peaks of $ZnWO_4$/CuO (6%) do not shift in comparison with those of the $ZnWO_4$ nanoplates. These results indicate that $ZnWO_4$/CuO (6%) contains monoclinic $ZnWO_4$, and the crystalline structure of $ZnWO_4$ is not changed. However, from the XRD pattern of $ZnWO_4$/CuO (6%), none of the diffraction peaks assigned to CuO or other Cu species can be observed. Because the peak positions of $ZnWO_4$/CuO (6%) do not shift with respect to the JCPDS card of monoclinic $ZnWO_4$ (JCPDS No. 89-0447), the Cu atoms are not incorporated into the $ZnWO_4$ lattice. In addition, as shown in Fig. 1, no broad peaks originating from an amorphous structure are present, which implies that the Cu species in $ZnWO_4$/CuO (6%) are crystalline compounds. As a result, this phenomenon should be attributed to the following. The Cu species uniformly distribute on the surface of $ZnWO_4$ in the form of small particles. Because these Cu species nanoparticles are very small, and the content of Cu species is low, we cannot observe any recognizable diffraction peaks.

The FT-IR spectrum of the $ZnWO_4$ nanoplates (Fig. S1a, ESI†) exhibits two bands appearing at 881 cm^{-1} and 826 cm^{-1}, arising from W–O asymmetric stretching.[44] Moreover, it can also be found that four bands at 712 cm^{-1}, 599 cm^{-1}, 471 cm^{-1} and 426 cm^{-1} exist, respectively. Therein, the bands at 712 cm^{-1} and 599 cm^{-1} might arise from Zn–O–W symmetric stretching. The band at 471 cm^{-1} can be ascribed to the asymmetric deformation of W–O bonds. The band at 426 cm^{-1} can be attributed to the asymmetric deformation of Zn–O bonds.[44] Fig. S1b (ESI†) shows the FT-IR spectrum of the CuO nanoparticles. From Fig. S1b (ESI†), we can observe the bands around 602 cm^{-1}, 508 cm^{-1} and 440 cm^{-1} which are related to the stretching vibration of Cu–O bonds.[45] The FT-IR spectrum of $ZnWO_4$/CuO (6%) is shown as Fig. S1c (ESI†). From Fig. S1c (ESI†), we can see that six bands at 886 cm^{-1}, 831 cm^{-1}, 715 cm^{-1}, 600 cm^{-1}, 467 cm^{-1} and 427 cm^{-1} exist, respectively. Here, the bands at 886 cm^{-1} and 831 cm^{-1} ought to originate from W–O asymmetric stretching. The bands at 715 cm^{-1} and 600 cm^{-1} might arise from Zn–O–W symmetric stretching. The bands at 467 cm^{-1} and 427 cm^{-1} should arise from the asymmetric deformation of W–O bonds and Zn–O bonds. Unfortunately, we cannot find any bands from CuO. This phenomenon may be ascribed to the low content of Cu species. However, the IR bands of $ZnWO_4$/CuO (6%) shift obviously in comparison with those of the $ZnWO_4$ nanoplates, implying that some Cu species are loaded on the $ZnWO_4$ nanoplates, and there exist some interactions between the $ZnWO_4$ nanoplates and the Cu species.

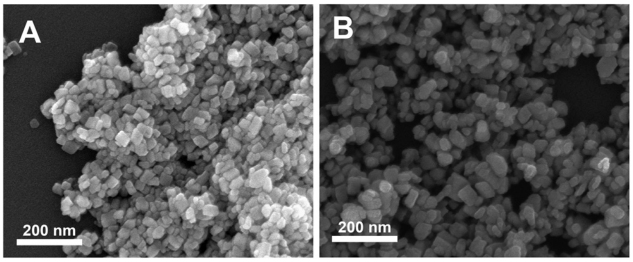

Fig. 2 SEM images of (A) the $ZnWO_4$ nanoplates and (B) $ZnWO_4$/CuO (6%).

Fig. 2A displays the scanning electron microscope (SEM) image of the $ZnWO_4$ nanoplates. From Fig. 2A, the $ZnWO_4$ nanoplates are clearly observed. These nanoplates adopt a quasi-rectangle morphology. Their lateral dimensions are approximately 40 nm × 30 nm. The transmission electron microscope (TEM) image of the $ZnWO_4$ nanoplates (Fig. 3A) also confirms the formation of nanoplates. Besides, we can also see from the TEM image of the $ZnWO_4$ nanoplates that these nanoplates are quite thin. These results certify that $ZnWO_4$ nanoplates have been obtained according to the above-mentioned procedure. Furthermore, the SEM image (Fig. 2B) and the TEM image (Fig. 3B) of $ZnWO_4$/CuO (6%) show that the morphology of $ZnWO_4$/CuO (6%) is almost the same as that of $ZnWO_4$ nanoplates, except that some small granular subunits appear on the surface of the $ZnWO_4$ nanoplates. This suggests that Cu species are introduced on the surface of $ZnWO_4$ in the form of small particles. Fig. 3C shows the high-resolution transmission electron microscope (HRTEM) image of $ZnWO_4$/CuO (6%). As can be seen from Fig. 3C, some nanoparticles can be resolved distinctly. The diameter of these nanoparticles is about 5 nm. Meanwhile, an interface can be clearly distinguished between the nanoparticles and the $ZnWO_4$ matrix. Besides, Fig. 3C also shows that some lattice stripes are present. Therein, for the lattice stripes which appear on the nanoparticles, the distance between two adjacent planes is about 0.231 nm, which corresponds to the (200) plane of monoclinic CuO (JCPDS No. 48-1548).[46] For the other lattice fringes, the interplanar spacing is about 0.203 nm, corresponding to the (112) plane of $ZnWO_4$ (JCPDS No. 89-0447). On account of the results above, we can deduce that the final product obtained is $ZnWO_4$ nanoplates loaded with CuO nanoparticles.

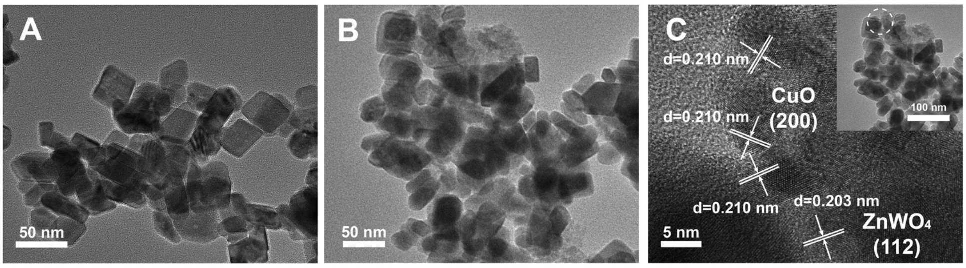

Fig. 3 TEM images of (A) the $ZnWO_4$ nanoplates and (B) $ZnWO_4$/CuO (6%), and the HRTEM image of (C) $ZnWO_4$/CuO (6%) (inset is the corresponding TEM image).

Fig. 4 and Fig. S2 (ESI†) show the X-ray photoelectron spectra (XPS) of $ZnWO_4$/CuO (6%). As shown in the survey spectrum (Fig. S2, ESI†), the characteristic XPS peaks assigned to Zn, W, Cu, O, and C can be found. Here, the signal of C might originate from the residues of the organic reagents used in the preparation process. This result confirms that the final product obtained is composed of Zn, W, Cu and O elements. Fig. 4A displays the high-resolution XPS spectrum of Zn 2P. As shown in Fig. 4A, two XPS peaks (1021.5 eV and 1044.6 eV) are present, which might be attributed to the Zn $2p_{3/2}$ peak and the Zn $2p_{1/2}$ peak of Zn^{2+} of $ZnWO_4$.[47] Moreover, we can find that these XPS peaks shift to higher binding energies in comparison with those of the $ZnWO_4$ nanoplates (Fig. S3A, ESI†), suggesting that there exist some interactions between the $ZnWO_4$ nanoplates and the CuO nanoparticles. Fig. 4B exhibits the high-resolution XPS spectrum of W 4f. As shown in Fig. 4B, two XPS peaks exist at 35.1 eV and 37.2 eV. They ought to be the W $4f_{7/2}$ peak and the W $4f_{5/2}$ peak of the W^{6+} oxidation state.[48] The high-resolution XPS spectrum of O 1s (Fig. 4C) shows that a broad peak accompanied with a shoulder peak appears around 530 eV. This broad peak can be decomposed into two peaks which are at 530.1 eV and 531.1 eV. Here, the peak at 530.1 eV

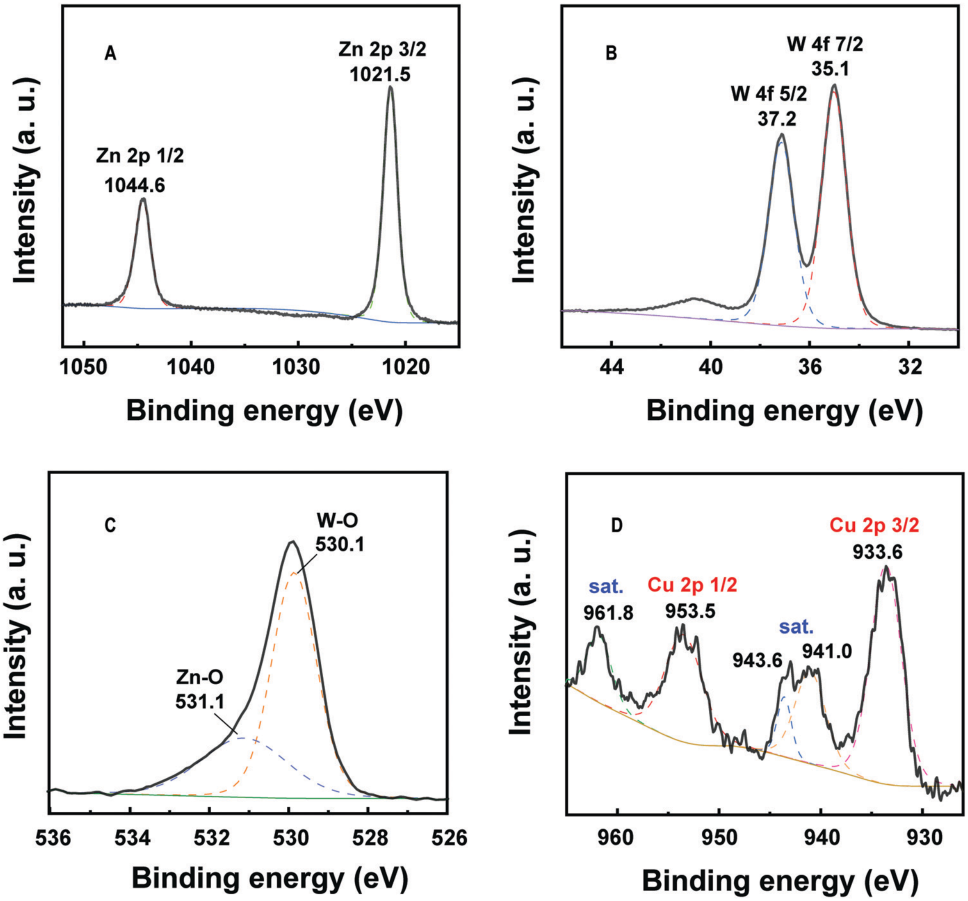

Fig. 4 XPS spectra of $ZnWO_4$/CuO (6%): (A) Zn 2p, (B) W 4f, (C) O 1s and (D) Cu 2p high-resolution XPS spectra (solid) and curve-fitting analysis (dot line) of the states of Zn, W, O, and Cu.

may be ascribed to the W–O bond in $ZnWO_4$. The peak at 531.1 eV may originate from the Zn–O bond in $ZnWO_4$.[49] Fig. 4D demonstrates the high-resolution XPS spectrum of Cu 2p. As shown in Fig. 4D, five peaks appear at 933.6 eV, 941.0 eV, 943.6 eV, 953.5 eV, and 961.8 eV, respectively. Therein, the peaks at 933.6 eV and 953.5 eV ought to be the Cu $2p_{3/2}$ peak and Cu $2p_{1/2}$ peak of CuO. The peaks at 941.0 eV, 943.6 eV, and 961.8 eV ought to be characteristic shakeup satellite peaks of CuO.[50–52] Similarly, we can also observe that these XPS peaks shift to a higher binding energy in comparison with those of the CuO nanoparticles (Fig. S3C, ESI†). This phenomenon indicates again that there are some interactions between the $ZnWO_4$ nanoplates and the CuO nanoparticles. Furthermore, we can observe from the elemental mappings of $ZnWO_4$/CuO (6%) (Fig. S4, ESI†) that the distribution of Zn and W elements is uniform, and their distribution boundaries coincide with the edges of the $ZnWO_4$ nanoplates shown in the energy-filtered TEM photograph (Fig. S4A, ESI†). Besides, the distribution of Cu is also homogeneous. These results imply that the CuO nanoparticles are homogeneously loaded on the surface of the $ZnWO_4$ nanoplates. Combined with the XRD, FT-IR, SEM, TEM and XPS results, it can be concluded that $ZnWO_4$ nanoplates loaded with CuO nanoparticles were successfully prepared according to the above-mentioned procedure. Furthermore, the distribution of CuO is homogeneous on the $ZnWO_4$ nanoplates.

In a general way, efficient photocatalysts usually possess a large specific surface area. Hence, the Brunauer–Emmett–Teller (BET) specific surface area of $ZnWO_4$/CuO (6%) was evaluated based on its N_2 gas adsorption isotherm. This result indicates that the specific surface area of $ZnWO_4$/CuO (6%) is large. Its specific surface area is up to 26.5 m^2 g^{-1}, implying that we can prepare an efficient photocatalyst using $ZnWO_4$/CuO.

Optical properties

Fig. S5 (ESI†) shows the UV-vis spectra of the $ZnWO_4$ nanoplates, the CuO nanoparticles and $ZnWO_4$/CuO (6%). As shown in Fig. S5 (ESI†), the $ZnWO_4$ nanoplates exhibit an absorption edge at 375 nm and poor absorption in the visible-light region. This UV absorption edge corresponds to the trans-band light absorption of $ZnWO_4$, and the band gap of the $ZnWO_4$ nanoplates is about 3.30 eV, which coincides with that reported previously.[20] This result indicates that the $ZnWO_4$ nanoplates cannot efficiently absorb visible light. In contrast, $ZnWO_4$/CuO (6%) possesses obviously enhanced light absorption in the visible light region besides a strong absorption band whose edge is around 375 nm. From Fig. S5 (ESI†), we can see that the CuO nanoparticles exhibit high absorbance in the range of 260–800 nm, suggesting that the CuO nanoparticles can efficiently absorb light in a wide region. Therefore, we can conclude that the strong visible absorption of $ZnWO_4$/CuO (6%) should be ascribed to the introduction of CuO nanoparticles. This phenomenon may originate from the electron transfer between the CuO nanoparticles and the $ZnWO_4$ nanoplates.[53]

Photocatalytic behavior of EY–$ZnWO_4$/CuO under illumination with various light intensities

Fig. 5A exhibits the kinetic curves of H_2 evolution in the presence of EY–$ZnWO_4$/CuO (6%), the EY sensitized $ZnWO_4$ nanoplates (EY–$ZnWO_4$), $ZnWO_4$/CuO (6%) or the $ZnWO_4$ nanoplates. As shown in Fig. 5A, the photocatalytic activity of the $ZnWO_4$ nanoplates is very weak. During 13 h irradiation, the mean H_2 evolution rate is only 0.023 mmol g^{-1} h^{-1}. This phenomenon might be attributed to fast recombination of photo-induced electron–hole pairs as well as feeble absorption in the visible region. In contrast, EY–$ZnWO_4$/CuO (6%) exhibits a dramatic photocatalytic performance for H_2 generation. During the first 4 h irradiation, the mean H_2 evolution rate is as high as 4.9 mmol g^{-1} h^{-1}, which is 196 times the H_2 evolution rate over the $ZnWO_4$ nanoplates (0.025 mmol g^{-1} h^{-1}). Moreover, the H_2 evolution rate basically remains unchanged during the first eight hours. Although the H_2 evolution rate then begins to gradually slow down, it is still up to 1.5 mmol g^{-1} h^{-1} after

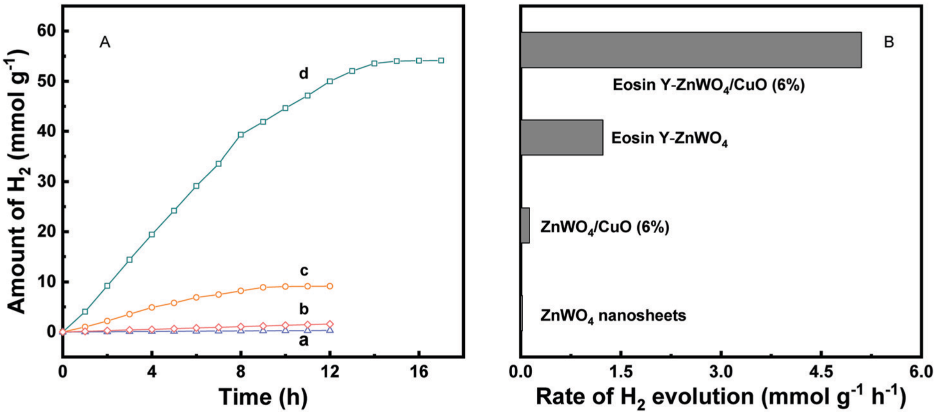

Fig. 5 (A) Time-courses of photocatalytic H_2 evolution in the presence of (a) $ZnWO_4$ nanoplates, (b) $ZnWO_4$/CuO (6%), (c) EY–$ZnWO_4$ and (d) EY–$ZnWO_4$/CuO (6%) (the $ZnWO_4$ nanoplates or $ZnWO_4$/CuO (6%) 5 mg, EY 40 mg, triethanolamine aqueous solution 60 mL 8.3 vol%, pH 10.6, temperature 10 °C, light intensity 100 mW cm^{-2}). (B) H_2 evolution rates in the presence of $ZnWO_4$ nanoplates, $ZnWO_4$/CuO (6%), EY–$ZnWO_4$ and EY–$ZnWO_4$/CuO (6%) (the $ZnWO_4$ nanoplates or $ZnWO_4$/CuO (6%) 5 mg, EY 40 mg, triethanolamine aqueous solution 60 mL 8.3 vol%, pH 10.6, temperature 10 °C, irradiation time 4 h, light intensity 100 mW cm^{-2}).

Table 1 Comparison of H_2 evolution over various photocatalysts

Photocatalyst	Light source	H_2 evolution rate (mmol g^{-1} h^{-1})	Ref.
EY–$ZnWO_4$/CoS	5 W LED lamp	7.12	20
$ZnWO_4$/ZnF_2O_4 composite	250 W metal halide lamp	2.8	23
Pt/N-doped $ZnWO_4$ nanorods	Sunlight	5.8	54
$ZnWO_4$/CdS composite	300 W Xe lamp	0.5	55
$ZnIn_2S_4$/$In(OH)_3$/$ZnWO_4$	300 W Xe lamp	1.03	56
Ag/$AgVO_3$/g-C_3N_4	500 W halogen lamp	3.57	57
EY-$ZnWO_4$/CuO	500 W Hg lamp	5.08	This work

14 h irradiation. These results illustrate that the photocatalytic performance of $ZnWO_4$ can be obviously boosted due to introduction of EY and CuO. EY–$ZnWO_4$/CuO (6%) not only possesses dramatic photocatalytic activity, but can also maintain the high photocatalytic activity for a period. Besides, its quantum yield (QE) and solar-to-hydrogen (STH) conversion efficiency are about 0.003% and 0.015% at 450 nm, respectively. Compared with the photocatalysts reported previously, EY–$ZnWO_4$/CuO (6%) also exhibits comparable activity (Table 1). Therefore, it can be concluded that EY–$ZnWO_4$/CuO is an efficient photocatalytic system for H_2 evolution.

Fig. 6 exhibits the effect of light intensity on the photocatalytic performance of EY–$ZnWO_4$/CuO (6%). As shown in Fig. 6, the H_2 evolution rate is obviously reduced as the light intensity is weakened. Even so, EY–$ZnWO_4$/CuO (6%) still exhibits satisfactory photocatalytic performance (0.53 mmol g^{-1} h^{-1}) under weak illumination (10 mW cm^{-2}). Moreover, when the light intensity is weakened from 100 mW cm^{-2} to 10 mW cm^{-2}, we find that EUF of EY–$ZnWO_4$/CuO (6%) (Table 2) remains basically unchanged, and a good linear relationship (R^2 = 0.99) exists between the H_2 evolution rate and the light intensity. These results indicate that the photocatalytic reaction should be quasi-first-order towards the incident photons.[11,12] The photocatalytic activity of EY–$ZnWO_4$/CuO (6%) doesn't rely on the incident light intensity. The decline in the H_2 evolution rate

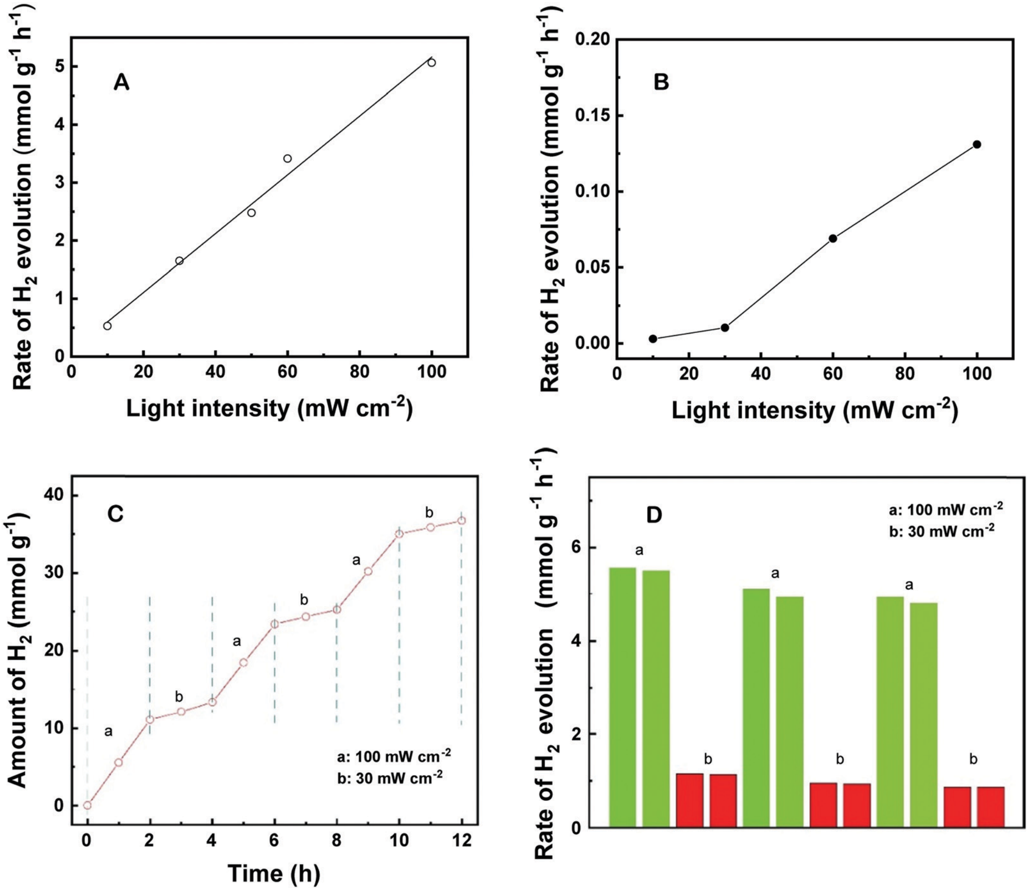

Fig. 6 (A) Effect of light intensity on the photocatalytic performance of EY–$ZnWO_4$/CuO (6%). (B) Effect of light intensity on the photocatalytic performance of $ZnWO_4$/CuO (6%). (C) Time-course of photocatalytic H_2 evolution in the presence of EY–$ZnWO_4$/CuO (6%) when the incident light intensity is periodically strengthened or weakened. (D) Corresponding H_2 evolution rate when the incident light intensity is periodically strengthened or weakened ($ZnWO_4$/CuO (6%) 5 mg, EY 40 mg, triethanolamine aqueous solution 60 mL 8.3 vol%, pH 10.6, temperature 10 °C, irradiation time 4 h).

Table 2 EUF of EY–$ZnWO_4$/CuO (6%) and $ZnWO_4$/CuO (6%) under illumination with various light intensities

Light power density ($mW\ cm^{-2}$)	EUF of EY–$ZnWO_4$/CuO (6%) ($\mu mol\ g^{-1}\ h^{-1}\ mW^{-1}$)	EUF of $ZnWO_4$/CuO (6%) ($\mu mol\ g^{-1}\ h^{-1}\ mW^{-1}$)
100	0.29	0.0073
60	0.32	0.0065
50	0.28	
30	0.31	0.0019
10	0.30	0.0017

ought to be attributed to the decreasing of the number of incident photons. In contrast, EUF of $ZnWO_4$/CuO (6%) decreases obviously as the light intensity is weakened. We cannot observe any linear relationship between the H_2 evolution rate and the light intensity. This phenomenon indicates that the light intensity-independent energy utilization of EY–$ZnWO_4$/CuO (6%) might originate from the sensitization of EY. Furthermore, from Fig. 6, it can be found that as the incident light intensity is periodically strengthened or weakened, the efficiency of hydrogen-production of EY–$ZnWO_4$/CuO (6%) increases or decreases, and the response speed is very fast. When the incident light intensity is strengthened, the rate of H_2 evolution increases at once. Similarly, just weakening the incident light intensity causes the rate of H_2 evolution to decrease at once. Moreover, as the light intensity cycles, the efficiency of hydrogen-production can be almost completely recovered if the incident light intensity returns to its initial state. Therefore, it can be concluded that EY–$ZnWO_4$/CuO (6%) is an efficient photocatalyst whose energy utilization is independent on light intensity, and has enormous potential of application in the field of sunlight driven H_2 production.

Effect of CuO content

Fig. S6 (ESI†) shows the effect of CuO content on H_2 evolution. From Fig. S6 (ESI†), it can be observed that the H_2 evolution rate gradually increases as the CuO content increases from 0.6 to 6%, and thereafter begins to decrease with increasing CuO content. The optimal content of CuO is 6%. We speculate that the CuO nanoparticles might serve as charge transferring sites and/or active sites in the photocatalytic process. When more CuO nanoparticles are loaded, the active sites would increase. Thus, the photocatalytic activity of EY–$ZnWO_4$/CuO is enhanced. However, the efficient contact between the CuO nanoparticles and the $ZnWO_4$ nanoplates may decrease as the content of CuO increases, which is unfavorable for the electron transfer between the CuO nanoparticles and the $ZnWO_4$ nanoplates. As a result, when the content of CuO is more than 6%, the H_2 evolution rate decreases.

Effect of pH on H_2 evolution

Fig. S7 (ESI†) shows the effect of the pH of the TEOA solution on H_2 evolution. From Fig. S7 (ESI†), we can observe that the amount of hydrogen produced increases when the pH value increases from 7 to 10.6. Afterwards, the amount of hydrogen produced decreases as pH increases. When the pH is 10.6, the rate of H_2 evolution is the fastest. One possible explanation is that the protonation of TEOA would be enhanced with decreasing pH. The electrons of the protonated TEOA molecules cannot migrate to the excited state of EY so that the oxidized EY molecules cannot be restored in time.[20] On the other hand, the thermodynamic driving force for H_2 evolution would be weakened with increasing pH. As a result, the rate of H_2 evolution increases when the pH value increases from 7 to 10.6. Subsequently, the amount of hydrogen produced would decrease if the pH value further increases.

Role of CuO nanoparticles

At first, it can be discovered from Fig. 5 that the photocatalytic performance of the $ZnWO_4$ nanoplates is significantly boosted when CuO nanoparticles are loaded on the $ZnWO_4$ nanoplates. The H_2 evolution rate over $ZnWO_4$/CuO (6%) is 0.13 mmol g^{-1} h^{-1}, which is 5.2 times the H_2 evolution rate over the $ZnWO_4$ nanoplates. Similarly, EY–$ZnWO_4$/CuO (6%) can exhibit higher photocatalytic activity compared with EY–$ZnWO_4$. One possible explanation is that the recombination of a photo-induced electron–hole pair would be efficiently stifled due to the presence of CuO. Secondly, we investigate the photocatalytic performance of EY–$ZnWO_4$/CuO (6%) under UV light (200–400 nm), visible-infrared light (400–2500 nm) and UV-visible-infrared light (200–2500 nm), respectively. Meanwhile, the photocatalytic performances of the $ZnWO_4$ nanoplates, $ZnWO_4$/CuO (6%) and EY–$ZnWO_4$ were also evaluated. The experimental data are listed in Table 3. As shown in Table 3, the $ZnWO_4$ nanoplates and $ZnWO_4$/CuO (6%) do not show any photocatalytic activity for H_2 generation under visible-infrared light. Under UV irradiation, the photocatalytic performance of the $ZnWO_4$ nanoplates is obviously boosted due to the presence of CuO. This phenomenon indicates that CuO cannot sensitize $ZnWO_4$ although the adsorption of the $ZnWO_4$ nanoplates can be enhanced in the visible region due to the presence of CuO nanoparticles (see the UV-vis spectra of the $ZnWO_4$ nanoplates and $ZnWO_4$/CuO (6%) shown in Fig. S5, ESI†). The boosting of the photocatalytic performance of the $ZnWO_4$ nanoplates should be ascribed to high-efficiency separation of electron–hole pairs. Thirdly, the fluorescence spectra of $ZnWO_4$ nanoplates and $ZnWO_4$/CuO (6%) were measured (Fig. 7). As shown in Fig. 7, the fluorescence of $ZnWO_4$ is significantly quenched when CuO nanoparticles are present on the $ZnWO_4$ nanoplates.

Table 3 H_2 evolution rates under UV irradiation (200–400 nm), visible-infrared irradiation (400–2500 nm), and UV-vis-infrared irradiation (200–2500 nm)[a]

	H_2 evolution rate (mmol g^{-1} h^{-1})		
Sample	UV	Visible-infrared	UV-vis-infrared
$ZnWO_4$ nanoplates	0.021	No detection	0.025
$ZnWO_4$/CuO (6%)	0.13	No detection	0.12
EY–$ZnWO_4$	0.82	0.44	1.23
EY–$ZnWO_4$/CuO (6%)	3.89	1.47	5.07

[a] $ZnWO_4$ nanoplates or $ZnWO_4$/CuO (6%) 5 mg, EY 40 mg, triethanolamine aqueous solution 60 mL 8.3 vol%, pH 10.6, temperature 10 °C, irradiation time 4 h, light intensity 100 mW cm^{-2}.

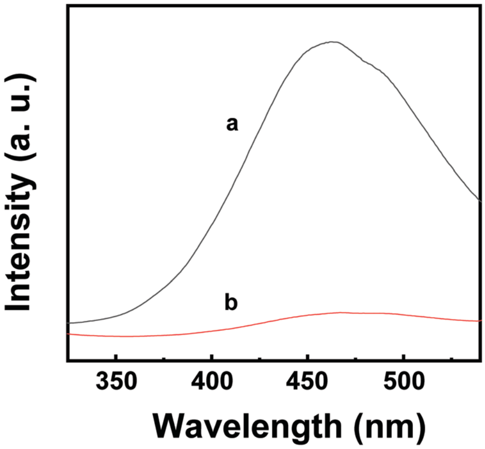

Fig. 7 Fluorescence spectra of (a) the $ZnWO_4$ nanoplates and (b) $ZnWO_4$/CuO (6%) (excitation wavelength 285 nm).

The phenomenon above ultimately confirms that electron–hole pair recombination would be efficiently suppressed due to the introduction of CuO. Futhermore, Fig. 8A demonstrates the transient photocurrent–time curves on the electrodes modified with the $ZnWO_4$ nanoplates and the electrodes modified with $ZnWO_4$/CuO (6%) in the presence or absence of EY. As shown in Fig. 8A, the photocurrent on the $ZnWO_4$/CuO (6%) modified electrode is stronger than that on the electrode modified with $ZnWO_4$ nanoplates whether EY is present or not. Once again, this result confirms that the electron–hole pair separation would be obviously enhanced when the CuO nanoparticles are present on the $ZnWO_4$ nanoplates. Therefore, we can speculate that the CuO nanoparticles serve as charge transferring sites and reactive sites in EY–$ZnWO_4$/CuO.

Role of EY

As shown in Fig. 5B, the photocatalytic performance of the $ZnWO_4$ nanoplates can also be obviously enhanced if EY is present. When EY is used, the H_2 evolution rate would be increased from 0.025 mmol g^{-1} h^{-1} to 1.23 mmol g^{-1} h^{-1}. This result indicates that EY is an efficient sensitizer for $ZnWO_4$. The enhancement of the photocatalytic performance of $ZnWO_4$ ought to be attributed to extension and reinforcement of the light absorption of $ZnWO_4$. Meanwhile, we can observe from Table 3 that both EY–$ZnWO_4$/CuO (6%) and EY–$ZnWO_4$ possess high photocatalytic activity under visible-infrared irradiation. This further confirms that EY is an efficient sensitizer for $ZnWO_4$. More interesting, both EY–$ZnWO_4$/CuO (6%) and EY–$ZnWO_4$ also exhibit much higher photocatalytic activity under UV light in comparison with $ZnWO_4$/CuO (6%) and the $ZnWO_4$ nanoplates. One possible explanation is that EY can efficiently absorb UV light as well as visible light (Fig. S5, ESI†). Hence, both the $ZnWO_4$ nanoplates and $ZnWO_4$/CuO (6%) can be sensitized by EY in the UV region. In light of the experimental results above, we can deduce that the dramatic photocatalytic activity of EY–$ZnWO_4$/CuO (6%) should be mainly attributed to the sensitization of EY.

Furthermore, it can be observed from Fig. 8A, when EY is present, that both the $ZnWO_4$ nanoplate coated electrode and the $ZnWO_4$/CuO (6%) coated electrode exhibit much stronger photocurrents in comparison with those in the absence of EY. And, in the presence of EY, we can find the strongest photocurrent on the $ZnWO_4$/CuO (6%) modified electrode. These phenomena indicate that the concentration of electrons on the surface of the $ZnWO_4$ nanoplates would obviously increase due to the sensitization of EY, implying that efficient tunneling would be realized in EY–$ZnWO_4$/CuO (6%). Fig. 8B shows the current–voltage curves on the $ZnWO_4$/CuO (6%) coated electrodes under irradiation when EY is absent or present. From Fig. 8B, we can find that when EY is present, the onset potential obviously shifts to a less negative potential by ~220 mV under forward bias, which indicates that the activation energy for the electron transfer between $ZnWO_4$ and CuO would be reduced due to the sensitization of EY.[12] One possible explanation is that when the $ZnWO_4$ nanoplates are sensitized by EY, the concentration of electrons on the surface of the $ZnWO_4$ nanoplates would increase so that

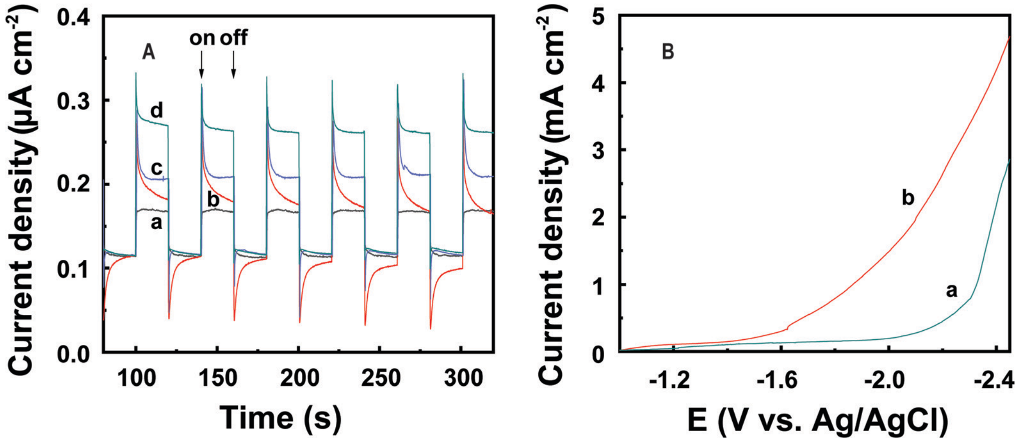

Fig. 8 (A) Transient photocurrent-time curves on (a) the $ZnWO_4$ nanoplate coated electrode in the absence of EY, (b) the $ZnWO_4$/CuO (6%) coated electrode in the absence of EY, (c) the $ZnWO_4$ nanoplate coated electrode in the presence of EY and (d) the $ZnWO_4$/CuO (6%) coated electrode in the presence of EY. (B) Voltage–current curves on the $ZnWO_4$/CuO (6%) coated electrode: (a) in the absence of EY and (b) in the presence of EY.

efficient tunneling can be realized in $ZnWO_4$/CuO (6%). As a result, the activation energy for the electron transfer between $ZnWO_4$ and CuO decreases.[12] This may be the reason why EY–$ZnWO_4$/CuO (6%) is an efficient photocatalyst whose energy utilization is independent of light intensity. Therefore, we speculate that EY acts as a light harvester to enhance the light absorption of $ZnWO_4$ in EY–$ZnWO_4$/CuO, and the light intensity-independent energy utilization of EY–$ZnWO_4$/CuO should be ascribed to the efficient sensitization of EY.

Discussion on reactive oxidative species

Fig. 9 shows the photocatalytic behavior of EY–$ZnWO_4$/CuO (6%) when scavengers for reactive oxidative species are present. As shown in Fig. 9, when isopropanol (scavenger for $^{\bullet}OH$), ammonium oxalate (scavenger for the hole) and benzoquinone (scavenger for $^{\bullet}O_2^-$) are added in the photocatalytic system separately, the H_2 evolution rate becomes noticeably slower. Benzoquinone exhibits the strongest inhibitory effect of the three. In contrast, L-tryptophan (scavenger for $^1O_2$) can hardly exhibit an inhibitory effect on the photocatalytic H_2 evolution. These phenomena suggest that there exist holes, $^{\bullet}OH$ radicals and $^{\bullet}O_2^-$ radicals in the photocatalytic process. Among the reactive oxidative species above, $^{\bullet}O_2^-$ radicals play a decisive role in the photocatalytic process and the photogenerated holes and $^{\bullet}OH$ radicals play non-negligible roles. However, prior to irradiation, O_2 was completely removed from the reactor. Therefore, the $^{\bullet}O_2^-$ radicals should originate from the photocatalytic water oxidation reaction. One possible explanation is that the photogenerated holes are not effectively trapped by TEOA, which leads to O_2 production on the $ZnWO_4$ nanoplates.

Photocatalytic mechanism of EY–$ZnWO_4$/CuO

In light of the above-mentioned results, we speculate that the photocatalytic mechanism of EY–$ZnWO_4$/CuO might be as follows (Scheme 2). Firstly, as EY–$ZnWO_4$/CuO is irradiated, the electrons of EY molecules jump from the occupied molecular orbitals to the unoccupied molecular orbitals. Meanwhile, the $ZnWO_4$ nanoplates absorb UV light. Afterwards, the electrons on the valence band (VB) of $ZnWO_4$ jump to its conduction band (CB). Secondly, the electrons of the excited EY molecules are injected into the CB of $ZnWO_4$. Thirdly, these photogenerated electrons migrate from the CB of $ZnWO_4$ to the CB of CuO because the position of CuO CB is more positive in comparison with that of $ZnWO_4$ (CuO is 0.1 V *vs.* NHE[53] and $ZnWO_4$ is −0.41 V *vs.* NHE[58]). As electrons accumulate in the CB of CuO, the Fermi level of CuO would shift to a negative potential.[59] Finally, on the CuO nanoparticles, water molecules are reduced to H_2 by the photogenerated electrons. On the other hand, oxidized EY molecules are regenerated by sacrificial reagent TEOA. Some holes are consumed by OH^- or the adsorbed water molecules to produce $^{\bullet}OH$ radicals or O_2 on the $ZnWO_4$ nanoplates. The O_2 molecules would immediately react with the photogenerated electrons to form $^{\bullet}O_2^-$ radicals. Subsequently, the other holes, $^{\bullet}OH$ radicals and $^{\bullet}O_2^-$ radicals irreversibly react with TEOA on the $ZnWO_4$ nanoplates. In this photocatalytic system, the CuO nanoparticles act as charge transferring sites and/or active sites. EY acts as a light harvester to extend and reinforce the light absorption of $ZnWO_4$. The remarkable photocatalytic performance of EY–$ZnWO_4$/CuO ought to be attributed to the extension and reinforcement of the light absorption of $ZnWO_4$ as well as efficient separation of the electron-hole pair. Besides, due to efficient sensitization of EY, the electron concentration on the surface of the $ZnWO_4$ nanoplates would increase so that efficient tunneling can be achieved in $ZnWO_4$/CuO. Thus, the energy barrier of the electron transfer between $ZnWO_4$ and CuO would be narrowed, resulting in EY–$ZnWO_4$/CuO exhibiting light intensity-independent energy utilization.

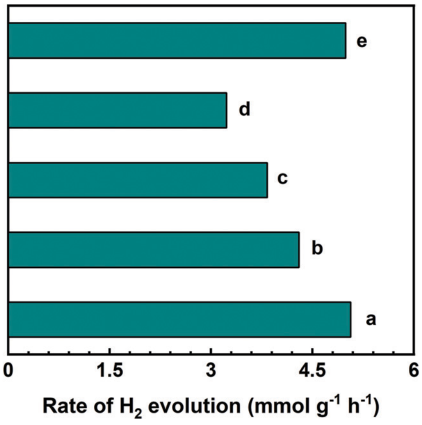

Fig. 9 Photocatalytic behavior of EY–$ZnWO_4$/CuO (6%) for H_2 evolution (a) in the absence of scavengers and in the presence of (b) iospropanol, (c) ammonium oxalate, (d) benzoquinone, and (e) L-tryptophan.

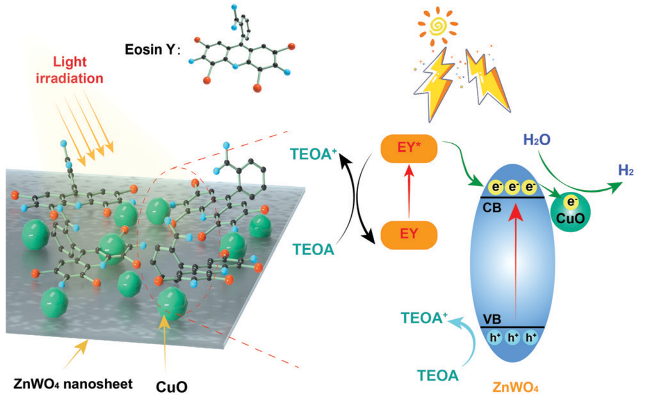

Scheme 2 Scheme showing the photocatalytic H_2 evolution over $ZnWO_4$/CuO when EY is present.

Regenerability of EY–$ZnWO_4$/CuO

The experimental results exhibit that the photocatalytic activity of EY–$ZnWO_4$/CuO (6%) would be gradually weakened until complete deactivation with prolonged irradiation time. On the other hand, the XRD pattern and the Cu 2p high-resolution XPS spectrum of the used $ZnWO_4$/CuO (6%) (Fig. S8, ESI†) are almost identical to those of the fresh $ZnWO_4$/CuO (6%). In contrast, the UV-vis spectra of the EY solution (Fig. S9, ESI†)

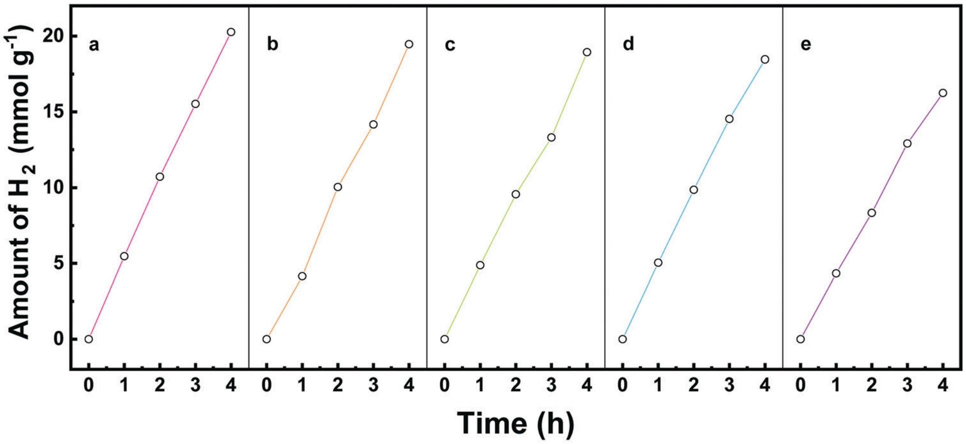

Fig. 10 Time-courses of photocatalytic H_2 evolution in the presence of (a) fresh EY–$ZnWO_4$/CuO (6%), (b) EY–$ZnWO_4$/CuO (6%) obtained in the first regeneration, (c) EY–$ZnWO_4$/CuO (6%) in the second regeneration, (d) EY–$ZnWO_4$/CuO (6%) obtained in the third regeneration, and (e) EY–$ZnWO_4$/CuO (6%) obtained in the fourth regeneration.

show that the absorption of EY would be weakened after irradiation in the presence of $ZnWO_4$/CuO (6%) and TEOA. These phenomena indicate that $ZnWO_4$/CuO (6%) possesses high chemical stability as well as satisfactory mechanical stability. The deactivation of EY–$ZnWO_4$/CuO (6%) ought to be ascribed to the photodegradation of EY. Therefore, it can be inferred that the photocatalytic activity of EY–$ZnWO_4$/CuO (6%) would be restored if degraded EY is replaced by fresh EY. *i.e.*, EY–$ZnWO_4$/CuO may possesses remarkable regenerability. In order to verify our assumption, the regenerability of EY–$ZnWO_4$/CuO (6%) was examined (Fig. 10). As shown in Fig. 10, the regenerability of EY–$ZnWO_4$/CuO (6%) is very satisfactory. In the case of the first regeneration, the photocatalytic activity of regenerated EY–$ZnWO_4$/CuO (6%) is almost same as that of the fresh EY–$ZnWO_4$/CuO (6%). Even though EY–$ZnWO_4$/CuO (6%) is regenerated four times, the regenerated EY–$ZnWO_4$/CuO (6%) retains about 80 percent of the photocatalytic activity of fresh EY–$ZnWO_4$/CuO (6%). These results confirm that EY–$ZnWO_4$/CuO (6%) is a reproducible, efficient photocatalyst for H_2 evolution. The attenuation in photocatalytic activity might be attributed to wastage of $ZnWO_4$/CuO (6%) during the regeneration and washing process.

Conclusions

In summary, we successfully fabricated a photocatalytic system containing EY, $ZnWO_4$ nanoplates and CuO nanoparticles. This photocatalytic system is an efficient photocatalyst with light intensity-independent energy utilization for H_2 evolution. Even under weak illumination its photocatalytic activity is still satisfactory. In addition, this photocatalytic system possesses remarkable regenerability. Here, the remarkable photocatalytic performance of EY–$ZnWO_4$/CuO ought to be attributed to two causes as follows. One is extension and reinforcement of the light absorption of $ZnWO_4$ ascribed to the efficient sensitization of EY. Another is high-efficiency separation of the electron-hole pair due to the introduction of CuO nanoparticles. Besides, the light intensity-independent energy utilization of EY–$ZnWO_4$/CuO should also be ascribed to the efficient sensitization of EY. Furthermore, it can be deduced that dye sensitization would be an effective strategy to develop a high-efficiency photocatalytic system with light intensity-independent energy utilization. This provides a new course for preparation of commercial photocatalysts which can be applied on a large scale in the field of sunlight-driven H_2 production.

Conflicts of interest

There are no conflicts to declare.

Acknowledgements

This work was financially supported by the National Natural Science Foundation of China (No. 21771125, 21606151).

References

1 C. Bie, J. Fu, B. Cheng and L. Zhang, *Appl. Surf. Sci.*, 2018, **462**, 606–614.
2 F. Dai, Y. Wang, X. Zhou, R. Zhao, J. Han and L. Wang, *Appl. Surf. Sci.*, 2020, **517**, 146161.
3 T. Hu, K. Dai, J. Zhang and S. Chen, *Appl. Catal., B*, 2020, **269**, 118844.
4 W. Li, S. Min, F. Wang and Z. Zhang, *Sustainable Energy Fuels*, 2020, **4**, 116–120.
5 L. Lu, B. Wu, W. Shi and P. Cheng, *Inorg. Chem. Front.*, 2019, **6**, 3456–3467.
6 X. Kong, Z. Peng, R. Jiang, P. Jia, J. Feng, P. Yang, Q. Chi, W. Ye, F. Xu and P. Gao, *ACS Appl. Nano Mater.*, 2020, **3**, 1373–1381.
7 F. Temerov, K. Pham, P. Juuti, J. M. Makela, E. V. Grachova, S. Kumar, S. Eslava and J. J. Saarinen, *ACS Appl. Mater. Interfaces*, 2020, **12**, 41200–41210.

8 D. Long, W. Chen, S. Zheng, X. Rao and Y. Zhang, *Ind. Eng. Chem. Res.*, 2020, **59**, 4549–4556.
9 D. Zhang, W. Cao, B. Mao, Y. Liu, F. Li, W. Dong, T. Jiang, Y.-C. Yong and W. Shi, *Ind. Eng. Chem. Res.*, 2020, **59**, 16249–16257.
10 Z. Chen, S. Yang, Z. Tian and B. Zhu, *Appl. Surf. Sci.*, 2019, **469**, 657–665.
11 Z. Wang, W. Qiao, M. Yuan, N. Li and J. Chen, *J. Phys. Chem. Lett.*, 2020, **11**, 2369–2373.
12 Z. Wang, W. Qiao, M. Yuan, N. Li and J. Chen, *J. Phys. Chem. Lett.*, 2020, **11**, 4644–4648.
13 S. Zhao, J. Xu, M. Mao, L. Li and X. Li, *J. Colloid Interface Sci.*, 2021, **583**, 435–447.
14 L. Han, Y. Lv, B. Li, H. Wen, H. Huang, Y. Guo and Z. Lin, *J. Colloid Interface Sci.*, 2020, **580**, 1–10.
15 B. W. Roehrich, R. Han and F. E. Osterloh, *J. Photochem. Photobiol., A*, 2020, **400**, 112705.
16 L. Yang, X. Bai, J. Shi, X. Du, L. Xu and P. Jin, *Appl. Catal., B*, 2019, **256**, 117759.
17 C. Ji, W. Wang, E.-S. M. El-Sayed, G. Liu, Y. Si, K. Su, Z. Ju, F. Wu and D. Yuan, *Appl. Catal., B*, 2021, **285**, 119782.
18 J. Shi, F. Chen, L. Hou, G. Li, Y. Li, X. Guan, H. Liu and L. Guo, *Appl. Catal., B*, 2021, **280**, 119385.
19 B. Li, Y. Zhang, F. Duanmu, Y. Shen, Z. Shen and S. Zhong, *Photochem. Photobiol. Sci.*, 2019, **18**, 1408–1418.
20 Z. Liu, J. Xu, Q. Liang, Y. Li and H. Yu, *J. Nanopart. Res.*, 2020, **22**, 114–125.
21 Y. Wu, S. Zhou, T. He, X. Jin and L. Lun, *Appl. Surf. Sci.*, 2019, **484**, 409–413.
22 P. F. S. Pereira, A. F. Gouveia, M. Assis, R. C. deOliveira, I. M. Pinatti, M. Penha, R. F. Goncalves, L. Gracia, J. Andres and E. Longo, *Phys. Chem. Chem. Phys.*, 2018, **20**, 1923–1937.
23 N. K. Veldurthi, N. K. Eswar, S. A. Singh and G. Madras, *Catal. Sci. Technol.*, 2018, **8**, 1083–1093.
24 H. He, Z. Luo, Z.-Y. Tang and C. Yu, *Appl. Surf. Sci.*, 2019, **490**, 460–468.
25 Y. Gao, Y. Huang, Y. Li, Q. Zhang, J. Cao, W. Ho and S. C. Lee, *ACS Sustainable Chem. Eng.*, 2016, **4**, 6912–6920.
26 D. P. Ojha and H. J. Kim, *Chem. Eng. Sci.*, 2020, **212**, 115338.
27 Y. Wu, S. Zhou, T. He, X. Jin and L. Lun, *Appl. Surf. Sci.*, 2019, **484**, 409–413.
28 P. Wang, L. Zong, Z. Guan, Q. Li and J. Yang, *Nanoscale Res. Lett.*, 2018, **13**, 33–42.
29 A. K. Ahmad, F. Nawaz, M. Yousaf, A. Shameem, M. S. Mahr, J. Iqbal, M. Shafique and M. A. Javed, *Russ. J. Phys. Chem. B*, 2020, **14**, 552–558.
30 S. E. Lee, A. Nasirian, Y. E. Kim, P. T. Fard, Y. Kim, B. Jeong, S. J. Kim, J. O. Baeg and J. Kim, *J. Am. Chem. Soc.*, 2020, **142**, 19142–19149.
31 Q. Liu, Z. Li, Q. Liu, C. Cheng, M. Song and C. Huang, *Appl. Surf. Sci.*, 2020, **514**, 146096.
32 M. Zhang, L. Qin, X. Feng, S.-Z. Kang and X. Li, *Colloids Surf., A*, 2021, **614**, 126123.
33 Y. Li, K. Yin, L. Wang, X. Lu, Y. Zhang, Y. Liu, D. Yan, Y. Song and S. Luo, *Appl. Catal., B*, 2018, **239**, 537–544.
34 H. Liu, M. Wang, X. Zhang, J. Ma and G. Lu, *Appl. Catal., B*, 2018, **237**, 563–573.
35 J. Xu, Y. Qi and L. Wang, *Appl. Catal., B*, 2019, **246**, 72–81.
36 J. Shi, F. Chen, L. Hou, G. Li, Y. Li, X. Guan, H. Liu and L. Guo, *Appl. Catal., B*, 2021, **280**, 119385.
37 H. Hou, M. Shang, F. Gao, L. Wang, Q. Liu, J. Zheng, Z. Yang and W. Yang, *ACS Appl. Mater. Interfaces*, 2016, **8**, 20128–20137.
38 H. Wang, Y. Wang, C. Jiang, K. Ye, X. He, C. Xue, Z. Yang, X. Zhou and H. Ji, *ACS Appl. Mater. Interfaces*, 2020, **12**, 2259–2268.
39 L. Zhu, H. Li, Z. Liu, P. Xia, Y. Xie and D. Xiong, *J. Phys. Chem. C*, 2018, **122**, 9531–9539.
40 H. Chen, W. Leng and Y. Xu, *J. Phys. Chem. C*, 2014, **118**, 9982–9989.
41 J. Ran, H. Chen, X. Bai, S. Bi, H. Jiang, G. Cai, D. Cheng and X. Wang, *Appl. Surf. Sci.*, 2019, **493**, 1167–1176.
42 M. Moradi, F. Hasanvandian, A. A. Isari, F. Hayati, B. Kakavandi and S. R. Setayesh, *Appl. Catal., B*, 2021, **285**, 119838.
43 M. Li, Q. Meng, S. Li, P. Li, Q. Zhu, B.-N. Kim and J.-G. Li, *Ceram. Int.*, 2019, **45**, 10746–10755.
44 M. Li, T. Takei, Q. Zhu, B.-N. Kim and J.-G. Li, *Inorg. Chem.*, 2019, **58**, 9432–9442.
45 C. Yang, X. Su, J. Wang, X. Cao, S. Wang and L. Zhang, *Sens. Actuators, B*, 2013, **185**, 159–165.
46 J. Song, L. Xu, C. Zhou, R. Xing, Q. Dai, D. Liu and H. Song, *ACS Appl. Mater. Interfaces*, 2013, **5**, 12928–12934.
47 Y. Wu, N. Luo and R. Xue, *ACS Omega*, 2020, **5**, 24318–24328.
48 H. Zhuang, W. Xu, L. Lin, M. Huang, M. Xu, S. Chen and Z. Cai, *J. Mater. Sci. Technol.*, 2019, **35**, 2312–2318.
49 G. Zhao, J. Zou, X. Chen, T. Zhang, J. Yu, S. Zhou, C. Li and F. Jiao, *Ind. Eng. Chem. Res.*, 2020, **59**, 6479–6487.
50 H. S. H. Mohamed, L. Wu, C.-F. Li, Z.-Y. Hu, J. Liu, Z. Deng, L.-H. Chen, Y. Li and B.-L. Su, *ACS Appl. Mater. Interfaces*, 2019, **11**, 32957–32968.
51 H. Guan, P. Cai, X. Zhang, Y. Zhang, G. Chen and C. Dong, *J. Mater. Chem. A*, 2018, **6**, 13668–13675.
52 W. Hao, L. Zhao, X. Li, L. Qin, S. Han and S.-Z. Kang, *Int. J. Hydrogen Energy*, 2021, **46**, 6461–6473.
53 Y.-T. Liao, Y.-Y. Huang, H. M. Chen, K. Komaguchi, C.-H. Hou, J. Henzie, Y. Yamauchi, Y. Ide and K. C.-W. Wu, *ACS Appl. Mater. Interfaces*, 2017, **9**, 42425–42429.
54 Y. A. Sethi, C. S. Praveen, R. P. Panmand, A. Ambalkar, A. K. Kulkarni, S. W. Gosavi, M. V. Kulkarni and B. B. Kale, *Catal. Sci. Technol.*, 2018, **8**, 2909–2919.
55 N. Zhang, D. Chen, B. Cai, S. Wang, F. Niu, L. Qin and Y. Huang, *Int. J. Hydrogen Energy*, 2017, **42**, 1962–1969.
56 J. Zhao, X. Yan, N. Zhao, X. Li, B. Lu, X. Zhang and H. Yu, *RSC Adv.*, 2018, **8**, 4979–4986.
57 M. F. R. Samsudin, C. Frebillot, Y. Kaddoury, S. Sufian and W.-J. Ong, *J. Environ. Manage.*, 2020, **270**, 110803.
58 X. Wang, S. Yu, Z.-H. Li, L.-L. He, Q.-L. Liu, M.-Y. Hu, L. Xu, X.-F. Wang and Z. Xiang, *Chem. Eng. J.*, 2021, **405**, 126922.
59 H. Hou, M. Shang, F. Gao, L. Wang, Q. Liu, J. Zheng, Z. Yang and W. Yang, *ACS Appl. Mater. Interfaces*, 2016, **8**, 20128–20137.